University of Amsterdam

UvA-DARE (Digital Academic Repository)

Uncertainty Estimation and Design Optimization of 2D Diffraction-Based Overlay Metrology Targets

Röhrich, R.; Oliveri, G.; Kovaios, S.; Tenner, V.T.; Den Boef, A.J.; Overvelde, J.T.B.; Koenderink, A.F.

DOI
10.1021/acsphotonics.0c00911

Publication date
2020

Document Version
Final published version

Published in
ACS Photonics

License
CC BY-NC-ND

Link to publication

Citation for published version (APA):
Röhrich, R., Oliveri, G., Kovaios, S., Tenner, V. T., Den Boef, A. J., Overvelde, J. T. B., & Koenderink, A. F. (2020). Uncertainty Estimation and Design Optimization of 2D Diffraction-Based Overlay Metrology Targets. *ACS Photonics*, *7*(10), 2765-2777. https://doi.org/10.1021/acsphotonics.0c00911

General rights
It is not permitted to download or to forward/distribute the text or part of it without the consent of the author(s) and/or copyright holder(s), other than for strictly personal, individual use, unless the work is under an open content license (like Creative Commons).

Disclaimer/Complaints regulations
If you believe that digital publication of certain material infringes any of your rights or (privacy) interests, please let the Library know, stating your reasons. In case of a legitimate complaint, the Library will make the material inaccessible and/or remove it from the website. Please Ask the Library: https://uba.uva.nl/en/contact, or a letter to: Library of the University of Amsterdam, Secretariat, Singel 425, 1012 WP Amsterdam, The Netherlands. You will be contacted as soon as possible.

UvA-DARE is a service provided by the library of the University of Amsterdam (https://dare.uva.nl)

Download date:11 Nov 2022

This is an open access article published under a Creative Commons Non-Commercial No Derivative Works (CC-BY-NC-ND) Attribution License, which permits copying and redistribution of the article, and creation of adaptations, all for non-commercial purposes.

ACS AUTHORCHOICE

ACS Photonics

pubs.acs.org/journal/apchd5 Article

Uncertainty Estimation and Design Optimization of 2D Diffraction-Based Overlay Metrology Targets

Ruslan Röhrich, Giorgio Oliveri, Stefanos Kovaios, Vasco T. Tenner, Arie J. den Boef, Johannes T. B. Overvelde, and A. Femius Koenderink*

Cite This: ACS Photonics 2020, 7, 2765–2777

Read Online

ACCESS | Metrics & More | Article Recommendations

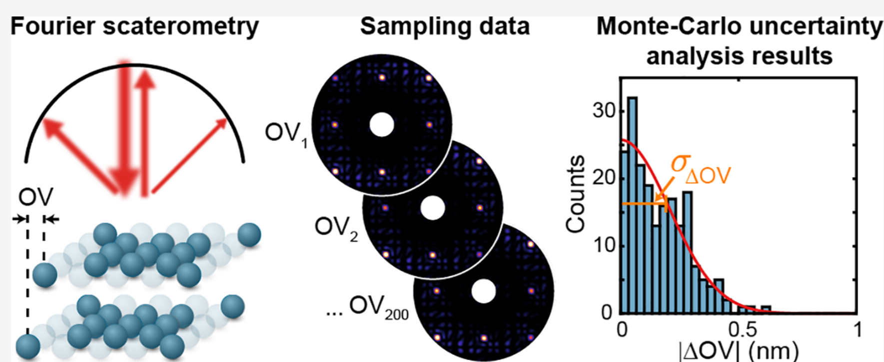

ABSTRACT: Scatterometry is an optical metrology technique in which light scattered from a specifically designed grating stack (overlay target) is measured in the far-field. Using 1D periodic overlay target designs, the technique has been shown to have nanometer-scale sensitivity to spatial misalignments of subsequent patterned layers, which are also known as overlay errors. However, while scatterometry is highly sensitive to overlay errors, multiple sources of systematic errors hinder its absolute accuracy. Here, we investigate how an extended version of scatterometry called Fourier scatterometry, in combination with more complex overlay target designs, can help addressing those challenges. To this end, we developed a statistical method that can determine the influence of 2D overlay targets on the overlay measurement uncertainty. We study periodic and deterministic aperiodic designs as well as designs that emerged from simulated annealing optimizations. Our results suggest that current overlay target designs could be augmented by more complex 2D designs to fulfill specific purposes, such as fabrication robustness and high sensitivity over a large overlay range.

KEYWORDS: *scatterometry, uncertainty analysis, optical nanometrology, optimization, Mie theory, dielectric metasurface*

Downloaded via UNIV AMSTERDAM on February 10, 2021 at 11:29:18 (UTC).
See https://pubs.acs.org/sharingguidelines for options on how to legitimately share published articles.

Current semiconductor manufacturing relies on highly accurate, real-time process monitoring techniques to achieve a high yield in modern integrated circuit fabrication, despite hundreds of necessary processing steps. One important type of metrology involves the measurement of spatial misalignments of subsequent patterned layers, which are also known as overlay (OV) errors. To ensure working devices, the OV error has to be smaller than a fraction of the minimum feature size. Continuously shrinking node sizes and increasing product stack complexity have reduced OV error tolerances down to only a few nanometers, which is why OV metrology could become a limiting factor for further progress of the industry.[1,2] A widely used OV metrology technique is diffraction-based overlay scatterometry (DBO),[3−5] in which diffraction patterns backscattered from two gratings that are stacked on top of each other are analyzed to infer the OV error. The idea is that for perfect alignment the OV target possesses a symmetric scattering signature, similar to a single grating. A spatial misalignment (|OV| > 0) results in an unbalanced Fourier-plane intensity distribution in the direction of the misalignment, as indicated in Figure 1a. Indeed, interference of light backscattered by the bottom and top gratings transduce the misalignment into an intensity difference between diffraction orders. For simple line gratings, for instance, the intensity in the 1st and −1st diffraction orders I_{+1} and I_{-1} can be used to construct the asymmetry signal $\Delta I = I_{+1} - I_{-1}$ that, for OV values much smaller than the grating pitch p, possesses a linear dependence on the OV error with a

Received: June 5, 2020
Published: August 26, 2020

© 2020 American Chemical Society

https://dx.doi.org/10.1021/acsphotonics.0c00911
ACS Photonics 2020, 7, 2765−2777

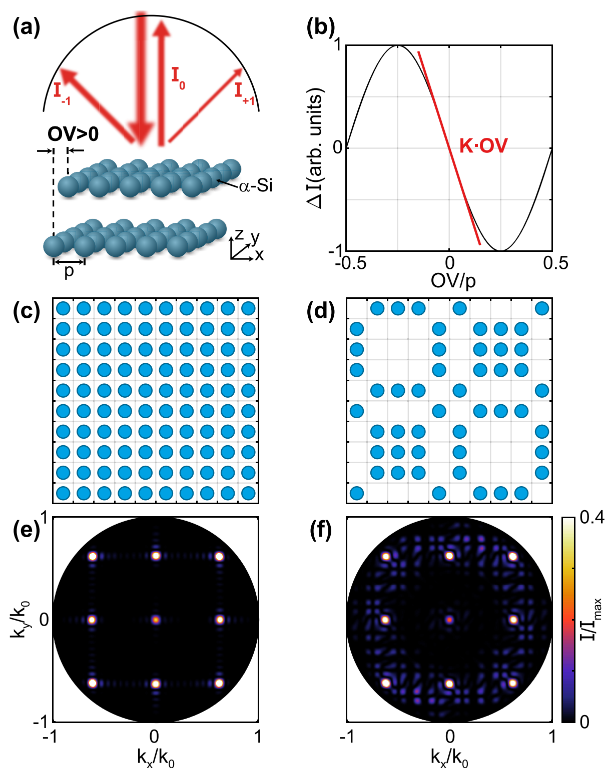

Figure 1. (a) Schematic of the measurement configuration in Fourier scatterometry, where scattered light is measured in the upper hemisphere above the sample. The spatial misalignment (OV error) between the top and bottom grating of the OV target causes an asymmetric backscattering signal. (b) This asymmetry signal ΔI, which is comprised of the difference between the 1st and −1st diffraction orders, has a linear dependence (shown in red) on OV at small OV values. (c, d) Square and aperiodic (Rudin-Shapiro) lattice designs. (e, f) Diffraction patterns generated by grating stacks with designs from (c) and (d) at OV = 0.

proportionality factor K, see Figure 1b. The exact value of K depends on the target structure and implementation of the type of scattering signature measurement and is, in practice, calibrated by measuring the asymmetry signal of two grating pairs with a programmed overlay offset.[4] Over the years, several types of scattering signature measurements have been demonstrated, including also spectroscopic and ellipsometric signals.[6−10]

In this work, we focus on Fourier scatterometry[10−14] in which a cone of light is scattered off a sample and collected by a microscope objective. Relaying the image of the objective back focal plane onto a 2D pixelated detector provides a direct mapping of scattering angles to image positions in a single shot measurement.[15] Notably, Fourier scatterometry is fast since no angle or frequency scanning is required and can be further enhanced to include polarization and phase resolution.[12−14] The fact that the full angle-dependent diffraction pattern is collected removes the limitation to only periodic OV target designs and allows the characterization of more complex (nonperiodic) 2D geometries. The purpose of this work is to explore whether 2D OV targets provide advantages for Fourier scatterometry in terms of OV accuracy, range of OV sensitivity and robustness in the face of measurement and fabrication noise. Figure 1c,e and d,f illustrate the rationale for this switch, demonstrating the diffraction patterns of a 2D periodic and a deterministic aperiodic OV target as calculated using a generalized Mie scattering modeling approach. Evidently 2D arrays offer a larger design space as compared to line gratings. The fact that many diffraction features appear means that there may be richer information in them, as compared to the simple asymmetry signal ΔI arising from the first diffraction orders. The 2D designs that we investigate borrow ideas from the branches of nanophotonics for photovoltaics, metasurfaces, and sensing[16−18] and, in particular, the study of deterministic aperiodic scattering structures.[19−22] In addition to periodic and deterministically aperiodic geometries, we considered geometries that emerged from numerical optimizations based on simulated annealing.[23] We followed a similar design search strategy, as described in ref 24. In general, numerical optimization is a popular tool to improve device performance in a wide range of fields, including mechanical design, nanophotonics, and optical metrology.[25−28]

In this paper we introduce a library-based Monte Carlo method, which aims to numerically characterize the performance of different OV target designs. To do this, we first build data sets containing calculated scattering patterns for a range of OV values and different OV target designs. For this we use generalized Lorentz-Mie Theory (GLMT) as a method that can deal with finite clusters of scatterers at very low computation time, yet exact position accuracy. Next, a low dimensional feature extraction is performed on the data sets by means of singular value decomposition (SVD). This type of approach originated in the field of face recognition, where it is referred to as "eigenface" technique.[29,30] The SVD results are used to construct libraries, which capture the effect of OV variation on the diffraction patterns of the different OV target types using only a few essential signatures. In subsequent Monte Carlo simulations we make use of these libraries to retrieve the OV values of new sampling data sets, which contain measurement or fabrication errors. Importantly, the prior knowledge that goes into building the library means that this OV retrieval is ultimately not limited by the optical resolution limit, but rather by the nonuniqueness of the inverse scattering problem or by unfitted fabrication and measurement fluctuations.[2,31] The merit of this paper thus includes both the analysis method and the provided comparison of OV target designs.

The paper is structured as follows. In the first part we present our numerical framework, which involves three main operations, namely, far-field scattering simulations, library creation, and Monte Carlo analysis. The following section deals with the OV target optimization procedure and its outcome. After this, we present our results on the dependence of OV measurement uncertainty on shot and fabrication noise. Finally, in Conclusion and Outlook we highlight the effectiveness of our technique and comment on how this kind of methodologies can help push the field of semiconductor metrology forward.

■ SIMULATION AND UNCERTAINTY ESTIMATION

Far-Field Scattering Simulation. Fourier-plane distributions of light backscattered from an OV target were simulated using the semianalytic Generalized Lorenz-Mie Theory (GLMT). This method allows us to compute scattered far-fields of finite-sized grating stacks at a high speed, while taking multiple scattering interactions into account to all orders and dealing with scatterer positions exactly, that is, without any discretization step. Although the method has the disadvantage that only assemblies of spheroidal scatterers in a homogeneous

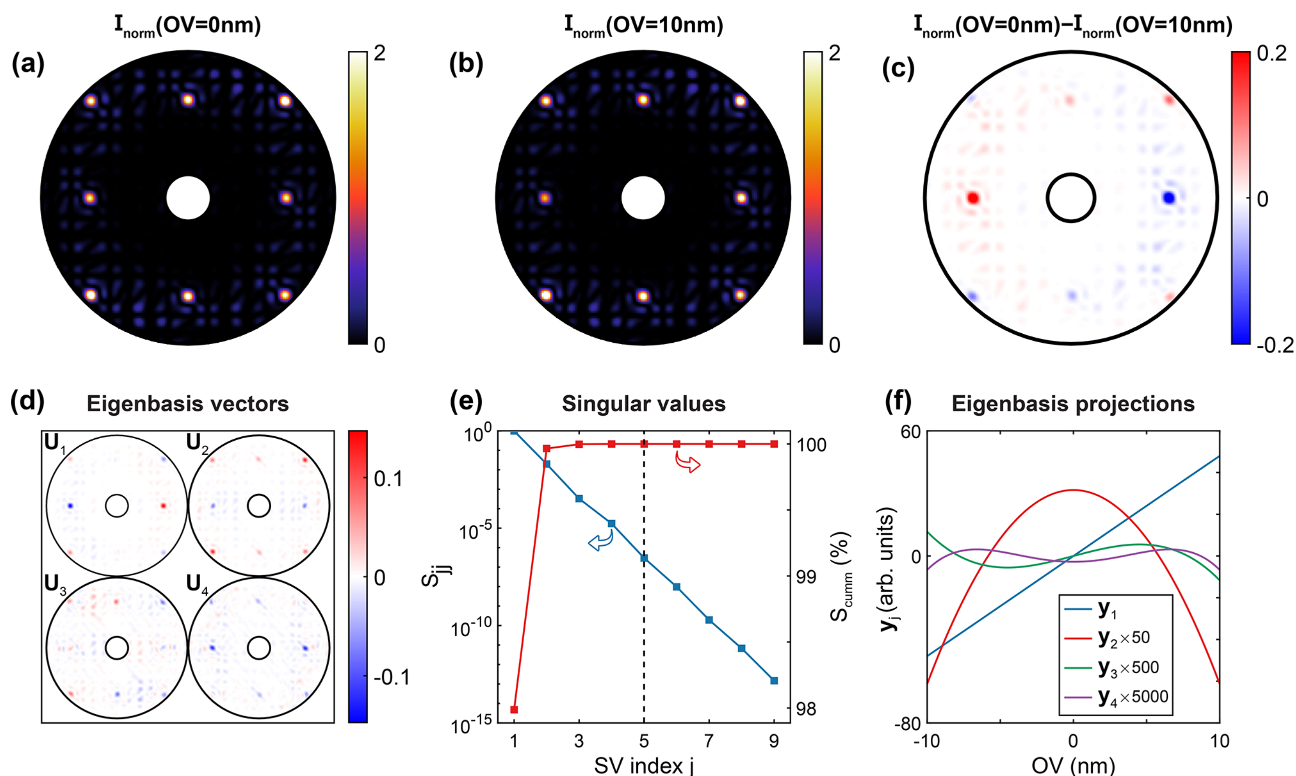

Figure 2. Library generation. (a, b) Normalized Fourier intensity maps for the Rudin-Shapiro OV target at an OV error of 0 and 10 nm. (c) Difference between (a) and (b). (d) Eigenbasis vectors and singular values obtained from the SVD of 101 far-field intensities with an OV value range of −10 to 10 nm. (e) The singular values S_{jj} are plotted in blue on a log-scale. The sum of the singular values is normalized to one. The red curve indicates the cumulative singular values S_{cum} in percent. (f) Projected coordinates of the library images in the SVD eigenspace as a function of OV. Note that the color scales in (a)−(c) are saturated at 80% of the maximum reflected intensity.

background medium can be dealt with, it offers large advantages over other approaches. In particular, RCWA (rigorous coupled wave analysis), which relies on a Fourier expansion of the dielectric constant, is a commonly used simulation method in scatterometry.[32,33] While it is known to be computationally efficient, it can not deal with finite truncations of infinite lattices or with aperiodic systems. Since in OV metrology one typically has targets of just 10 wavelengths across, the RCWA is of limited use unless one resorts to complex extensions to finite structures.[34] More computationally intensive mesh/grid discretization-based techniques like the Finite Element Method (FEM) and Finite Difference Time Domain (FDTD) method have been used for detailed studies of the signal formation process in scatterometry and have the advantage that more complex systems can be dealt with.[25,35,36] However, we have found that discretization is inherently problematic for OV metrology simulations, since the error in determining sub-nm OV from simulated data and libraries is limited by this discretization and not by the OV target, fabrication noise, or measurement scenario that one wishes to explore. While GLMT has not been used in the context of OV metrology it has the advantages of speed, accuracy, and requires no discretization of real space.[37,38]

To further decrease computation time, we only include up to dipolar electric and magnetic interactions into the Mie scattering model, which means that the spherical Bessel functions of the first kind in the Mie scattering formalism are expanded up to order 1. This approximation is tantamount to evaluating a fully retarded electrodynamic multiple scattering model for the overlay targets that takes into account electric and magnetic dipole responses of each particle but that neglects multipole corrections. Such approximations are typically used for small particles. We verified that an increase of the expansion order did not cause noticeable changes to the far-field radiation patterns of the OV targets. The arrays are excited by normally incident monochrome excitation of wavelength λ = 467.5 nm and polarized in the y direction. Both of the arrays consist of spherical amorphous silicon (α-Si) particles, which we model using dielectric data from ref 39, which leads to a refractive index of $n_{\alpha\text{-Si}}$ = 4.47 + i1.37 at λ = 467.5 nm. The background medium is assumed to be glass-like with a uniform refractive index of n_{SiO^2} = 1.5. These parameters have by no means been chosen to, for example, optimize the scattering cross section of the particles, with the rationale that OV metrology generally operates not with optimally chosen grating materials and dimensions, but within customer constraints. Since in modern technology nodes the available footprint for OV targets is limited, we chose an array design that takes up a total area of 4.8 × 4.8 μm^2. This is done by limiting our design space to a 10 × 10 grid with a pitch p = 500 nm, where every site can be filled or not filled by a nanoparticle with a radius r = 150 nm. Figure 1c,d shows two possible particle arrangements following this design constraint. The complete OV target consists of two identical gratings in the bottom and top layer, which are t = 400 nm apart. Any value of OV is introduced by shifting the top grating in the x-direction, as indicated in Figure 1a.

To mimick a practical optical set up scenario, a binary ring mask is applied to limit the scattering pattern to the angular range between NA = 0.225 and 1.42, where NA = n_{SiO_2} sin(θ)

is the numerical aperture and θ the polar angle. This is equivalent to using a high NA objective for capturing the first grating diffraction orders, with a beam block to remove directly reflected light, that is, zero-order light. Figure 2a shows such a masked Fourier-plane image for an example design studied in this work, a so-called Rudin−Shapiro target. Note that the full design space will be discussed later, and this design is merely an example. To make the comparison of the different array designs independent of the number of scatterers, we normalize the far-field intensity $|E_{\text{sim}}|^2$ to a constant photon count in the detected angular region. This normalization is computed as follows

$$I_{\text{norm}}(\text{OV}) = \frac{C_{\text{tot}}|E_{\text{sim}}(\text{OV})^2}{\sum_{k_x,k_y}|E_{\text{sim}}(\text{OV}_m)|^2} \quad (1)$$

where C_{tot} is the total photon count in the masked region and OV_m is the OV value producing the largest integrated photon count. C_{tot} can also be expressed using the average photon count C_{avg} as $C_{\text{tot}} = C_{\text{avg}}N_{\text{px}}$, where $N_{\text{px}} = 27636$ is the number of pixels of the ring mask. It should be noted that the choice of any particular normalization will affect the outcome of studies related to measurement noise. The normalization with a constant integrated photon count roughly assumes that the detected signal will be limited by a total source photon budget used for the measurements, as opposed to, for instance, normalizing images to a maximum count rate, which would be applicable if measurements were limited by the dynamic range of a detector. Figure 2a,b shows examples of normalized Fourier images I_{norm} of the Rudin−Shapiro target design at OV shifts of 0 and 10 nm. In the OV = 10 nm case, a slight asymmetry between the main grating orders on the left and right side arises due to the spatial misalignment of the two gratings. This asymmetry becomes more visible when we plot the difference between the two intensity patterns in Figure 2c. Further, Figure 2c shows that also many other Fourier plane components of lesser amplitude, introduced by the a-periodic nature of the target, show asymmetries and hence carry information relevant for OV error determination.

Library Generation Using SVD. Given a complex Fourier-plane distribution that varies with OV, as in Figure 2c, it is not obvious how to quantify the performance of a target in terms of OV metrology. To accomplish this task, we use a library search approach in combination with a feature extraction via singular value decomposition (SVD). Library-based techniques are known to be robust solutions to the scatterometry inverse problem with an OV accuracy that only depends on the library step size.[40] Here, to solve the Fourier scatterometry inverse problem, we construct a library using a series of Fourier images featuring the scattering of targets with a range of OV shifts, which we refer to as library images. To make the library more efficient, we perform a feature extraction via SVD, which is a technique well-known for its ability to greatly reduce the dimension of correlated data sets.[29] The SVD-based dimension reduction works by finding a new optimal orthonormal basis for the subspace containing all the library images of a particular OV target. Using this library eigenbasis, any new diffraction pattern of the OV target having an OV shift within the library range can be expressed by a linear combination without the loss of valuable information. This fact will subsequently allow the retrieval of OV values even if these values are not contained in the original data set.

In a first step, for each OV target, a series of N_{sim} library images are calculated featuring linearly increasing OV values within two different OV ranges, namely, [−10, 10] nm and [0, 125] nm. The images have a width and height of n = 201 pixels, from which N_{px} = 27636 pixels are used after a binary masking step, as described in the previous section. For the purpose of SVD, each of the N_{sim} library images is flattened to a column vector $\mathbf{f}_i$ and centered around their mean $\mathbf{f}_i^c = \mathbf{f}_i - \bar{\mathbf{f}}$, where $\bar{\mathbf{f}} = 1/N_{\text{sim}}\sum_i^{N_{\text{sim}}}\mathbf{f}_i$ is the average library image and i = 1, ..., N_{sim} is the library OV index. The centered vectors $\mathbf{f}_i^c$ form the columns of matrix $\mathbf{A} = [\mathbf{f}_1^c, \mathbf{f}_2^c, ..., \mathbf{f}_{N\text{sim}}^c]$. The SVD technique performs a factorization of matrix $\mathbf{A}$ ($n^2 \times N_{\text{sim}}$) of the form:

$$\mathbf{A} = \mathbf{U}\cdot\mathbf{S}\cdot\mathbf{V}^T \quad (2)$$

where T denotes the transpose operation. The orthonormal matrices $\mathbf{U}$ ($n^2 \times n^2$) and $\mathbf{V}^T$ ($N_{\text{sim}} \times N_{\text{sim}}$) contain the left-hand and right-hand singular vectors, and $\mathbf{S}$ ($n^2 \times N_{\text{sim}}$) is a rectangular matrix consisting of the singular values arranged in decreasing order along its diagonal.

Figure 2d,e shows an example of the SVD results for the Rudin−Shapiro target design in the OV range of [−10−10] nm. The first four singular vectors are shown in Figure 2d. Figure 2e shows the first nine singular values on a logarithmic scale (in blue), where the sum of all N_{sim} singular values is normalized to unity. By calculating the cumulative normalized singular values S_{cum} (shown in red and on a linear scale in Figure 2e), we can determine how accurately the first few components represent the signal. In this case, with only the first five eigenbasis components, the representation error of the full library data set is on the order of 10^{-6}%. In other words, the main OV-dependent behavior of the far-field scattering signal is almost fully captured by a few singular vectors, which suggests a high degree of correlation in the library data. This allows us to truncate the eigenbasis $\mathbf{U}$ without loss of valuable information, while greatly reducing computation load in subsequent analysis steps. The truncated eigenbasis $\tilde{\mathbf{U}}$ has a size of ($n^2 \times L$). The truncation indices L and the resulting errors (for the Rudin−Shapiro target) at both OV ranges are given in Table 1.

Table 1. Library Parameters[a]

OV range (nm)	N_{interp}	N_{sim}	$\text{OV}_{\text{sim,step}}$ (nm)	L	$1 - S_{\text{cumm}}(L)$ (%)
[−10, 10]	20001	101	0.2	5	9.9×10^{-7}
[0, 125]	125001	126	1	10	1.1×10^{-6}

[a]This table summarizes the number of interpolated and simulated OV shifts N_{interp} and N_{sim}, the simulated OV step size $\text{OV}_{\text{sim,step}}$, the singular value truncation index L, and the remaining commutative error due to truncation $1 - S_{\text{cumm}}(L)$ for the two investigated OV ranges.

An important property of the SVD is that the column vectors constituting $\tilde{\mathbf{U}}$ form an orthonormal basis of the column space of matrix $\mathbf{A}$. This allows to define a new coordinate space, wherein any diffraction pattern has as coordinate the linear expansion coefficients required to express $\mathbf{f}_i^c$ in $\tilde{\mathbf{U}}$. Thus, the eigenbasis coordinates of all the library images can be computed by projecting the centered images $\mathbf{f}_i^c$ onto a library eigenspace for every library OV index i = 1, ..., N_{sim} as

$$\mathbf{x}_i = \tilde{\mathbf{U}}^T\cdot\mathbf{f}_i^c \quad (3)$$

https://dx.doi.org/10.1021/acsphotonics.0c00911
ACS Photonics 2020, 7, 2765−2777

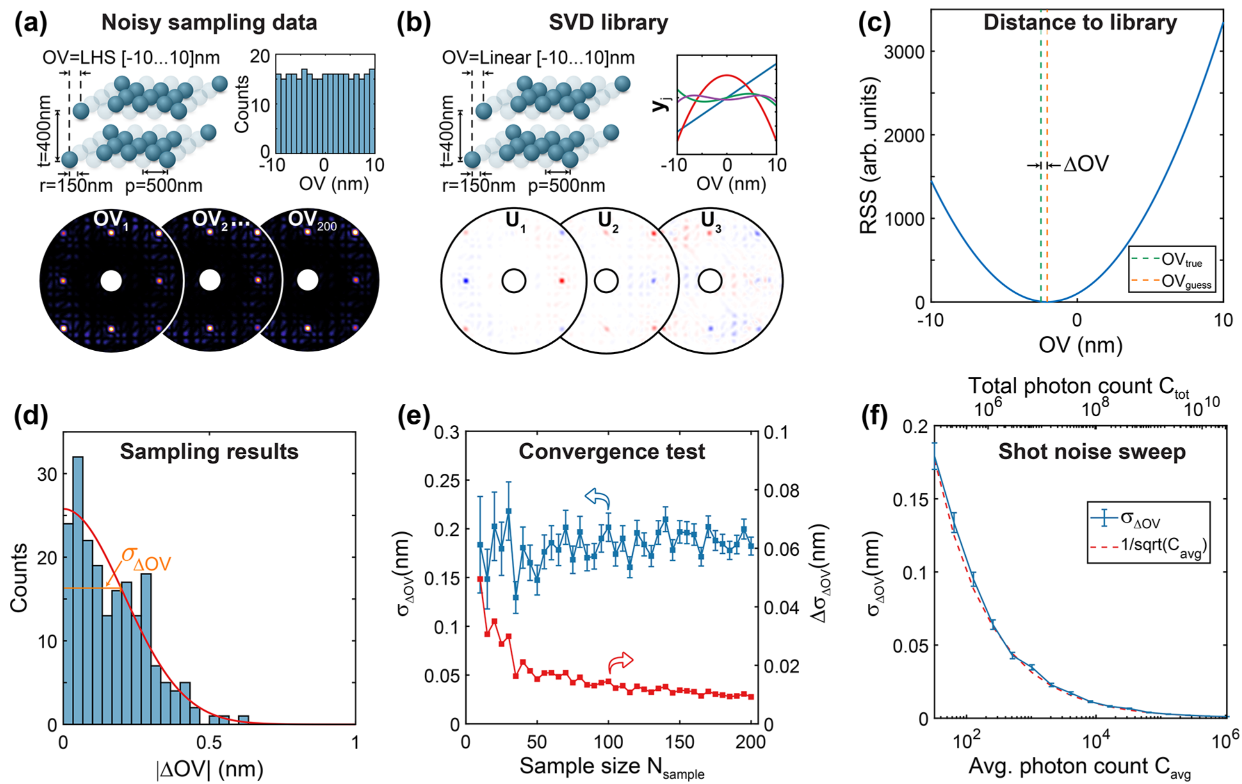

Figure 3. Monte Carlo method. (a) A 3D sketch showing a part of the Rudin−Shapiro target design and the parameters used in the sampling simulations. The histogram shows the distribution of the OV values, which follow a Latin-hypercube sampling. Below, sample images at three different OV values are shown. (b) The SVD library consisting of the eigenbasis vectors $\mathbf{U}$ and the interpolated OV-dependent library image projections $\mathbf{y}_i$. The library is created using the same parameters as the sampling data but with OV values varying linearly within the OV range of −10 to 10 nm. (c) RSS between projected sample image and the projected library images as a function of OV. (d) Histogram containing |ΔOV| values of 200 sample images. A fitted half-normal distribution (in red) with a standard deviation of $\sigma_{\Delta OV}$ = 0.19 ± 0.01 nm (indicated in orange). (e) $\sigma_{\Delta OV}$ (in blue) and its error (in red) for a varying number of included sampling simulations. (f) $\sigma_{\Delta OV}$ as a function of average photon count C_{avg} (bottom) and total photon count C_{tot} (top). The red dashed line indicates the inverse square root of C_{avg}. The sample images used for (a) and (c)−(e) contain shot noise corresponding to C_{avg} = 32.

The projected coordinates $\mathbf{x}_i$ form the columns of matrix $\mathbf{X}(N_{sim} \times L)$. The rows of matrix $\mathbf{X}$ will be referred to as $\mathbf{y}_j$. They reveal the OV-dependent behavior of the library images at the different eigenbasis indices $j = 1, ..., L$ and can be seen as an analogy to the asymmetry signal used in regular DBO. As an example, Figure 2f shows the first 4 rows of $\mathbf{X}$ for the Rudin−Shapiro data set, where $\mathbf{y}_j$, with $j > 1$, were magnified for clarity. Interestingly, $\mathbf{y}_1$, which contains projections onto the first and most significant SV component, shows a linear behavior as function of OV (shown in blue in Figure 2f). This observation is in line with the simple analytic expectation for DBO based on the asymmetry of the main first diffraction orders.[5] The fact that complex targets with more complex Fourier patterns carry more information is evident from the fact that also higher order eigenbasis coordinates show variations with overlay (see $\mathbf{y}_j$, with j = 2, 3, and 4 in Figure 2f). These nonlinear contributions, such as $\mathbf{y}_2$, aid OV sensitivity primarily at higher OV values, where their slope as a function of OV increases.

Finally, the continuous nature of $\mathbf{y}_j$ as a function of OV allows an interpolation to a much finer OV step size, which will greatly improve the accuracy of the library-based technique without the need of additional simulation runs. To this end, we perform cubic spline interpolations in MATLAB with a step size of $OV_{interp,step}$ = 0.001 nm for the libraries of both OV ranges. For the resulting number of interpolated OV shifts N_{interp}, see Table 1. A completed library for a particular OV target consists of the truncated eigenbasis $\tilde{\mathbf{U}}(n^2 \times L)$, the interpolated projected library coordinates $\mathbf{X}_{interp}(N_{interp} \times L)$ and the average library image $\bar{\mathbf{f}}$.

Uncertainty Estimation Using Monte Carlo Method. This section specifies how we use SVD libraries, which contain characteristic features extracted from the scattering profiles of particular OV targets, to directly map new scattering profiles (sample images) to specific OV values, provided that these OV values are within the library OV range. Further, we outline how to set up a Monte Carlo analysis to provide a numerical estimate of the OV retrieval uncertainty. In the context of metrology, Monte Carlo methods are often employed to determine measurement uncertainties.[41,42] More specifically, we use this method to study the robustness of a particular OV target design to shot noise and process variations in simulated Fourier scatterometry measurements. For this purpose, we first simulate N_{sample} Fourier images at randomly chosen sampling OV values. We refer to these as sampling images and ask how one would retrieve the OV corresponding to each sampling image. Figure 3a shows three sampling images and the parameters used for their simulation. The sampling OV values were drawn randomly according to the Latin-Hypercube Sampling (LHS) method.[43] We chose this sampling method, since LHS has been shown to have a superior convergence speed compared to other sampling techniques and has been successfully applied in the field of scatterometry.[44,45] An inset

in Figure 3a shows the LHS distributed OV values we used for the [−10, 10] nm OV range as a histogram.

Once an SVD library is created, determining the OV value of a sampling image can be treated as a feature recognition task. Figure 3b depicts the main ingredients of such a library, which is simulated with identical parameters as the sampling images, but with equidistant OV values spanning in total the same range as the sampling image set. The way the OV value recognition works is by projecting the sample image onto the library eigenspace and comparing this projection to each of the projections stored library. For this, the sample images are projected into the $\tilde{\mathbf{U}}$ subspace by calculating

$$\mathbf{x}_k = \tilde{\mathbf{U}}^T \cdot \mathbf{f}_k^c \tag{4}$$

where $\mathbf{f}_k^c = \mathbf{f}_k - \bar{\mathbf{f}}$ are the flattened and centered sample images with $k = 1, ..., N_{\text{sample}}$. Then, the OV estimation is performed by calculating the residual sum of squares (RSS) between the sample coordinate vector $\mathbf{x}_k$ and the library coordinate vectors $\mathbf{x}_i$ with $i = 1, ..., N_{\text{interp}}$ as

$$\text{RSS}_{i,k} = \sum_{j=1}^{L} (x_{k,j} - x_{i,j})^2 \tag{5}$$

The index i, which minimized eq 5, determines our OV estimate OV_{guess}. This approach corresponds to finding the library element with the minimal Euclidean distance to the sample image in the L-dimensional SVD coordinate space. An example RSS result as a function of OV is shown in Figure 3c. For this plot, a sampling image corrupted by shot noise corresponding to $C_{\text{avg}} = 32$ and with a "true" OV value of $\text{OV}_{\text{true}} = -2.48$ nm was used, which resulted in an OV estimate of $\text{OV}_{\text{guess}} = -2.06$ nm. Based on this estimate, we can calculate an OV estimate error as $\Delta\text{OV} = |\text{OV}_{\text{guess}} - \text{OV}_{\text{true}}|$, which in this example is 0.42 nm. Repeating this OV estimation for each of the N_{sample} sampling images allows to construct a histogram of such OV estimate errors, as shown in Figure 3d. The variance $\sigma_{\Delta\text{OV}}$ of this histogram is indicated in Figure 3d. It characterizes the accuracy of the OV estimation and is obtained by fitting a half-Gaussian to the ΔOV data. The fit also returns a standard deviation of $\sigma_{\Delta\text{OV}}$, which is a measure for the quality of the fit and to which we refer to as $\Delta\sigma_{\Delta\text{OV}}$. According to the central limit theorem $\Delta\sigma_{\Delta\text{OV}}$ should shrink with increasing sample size N_{sample}, and $\sigma_{\Delta\text{OV}}$ should converge for a large enough N_{sample}. To test this behavior and to determine an appropriate sample size, we performed convergence studies, as suggested in ref 46. Figure 3e shows such a convergence test, where $\sigma_{\Delta\text{OV}}$ and its standard deviation are plotted in blue as a function of sample size in the case of the Rudin−Shapiro target design and a photon budget set by $C_{\text{avg}} = 32$. In addition, Figure 3e shows $\Delta\sigma_{\Delta\text{OV}}$ in red (right y-axis) to demonstrate how it decreases with an increasing sample size. For studies with a varying photon budget, we found the results to converge sufficiently for a sample size of $N_{\text{sample}} = 200$ for the [−10, 10] nm OV range and $N_{\text{sample}} = 300$ for the [0, 125] nm OV range. For the fabrication noise studies, we used $N_{\text{sample}} = 300$.

In the results part, we will use the Monte Carlo technique described here to quantify the accuracy of OV determination for different OV target designs in the presence of noise in the sampling data, which will give us a measure for its noise robustness. For this we generate sampling data sets containing a variety of measurement and fabrication errors. As an example of such a study, Figure 3(f) shows the dependence of $\sigma_{\Delta\text{OV}}$ on shot noise for the Rudin-Shapiro target. The shot noise is controlled by varying the photon budget of the sample images. An increasing photon budget leads to less shot noise and therefore decreased $\sigma_{\Delta\text{OV}}$. Additionally, we can see that $\sigma_{\Delta\text{OV}}$ scales similarly to the inverse square root of the average photon budget C_{avg} (red dashed line).

Overlay Target Optimizations. In this section, we use the simulated annealing approach to find target designs that allow for the greatest OV sensitivity. In simulated annealing one needs to minimize a merit or cost function that ideally can be quickly evaluated to reduce total computation time. As the full SVD-based approach described in the last section requires significant computation time, we chose a cost function based on the correlation of the complex-valued far-fields at two different OV values. The cost function is calculated as follows

$$\Phi = \frac{2\langle E_{\text{OV}_1}, E_{\text{OV}_2}\rangle}{\langle E_{\text{OV}_1}, E_{\text{OV}_1}\rangle + \langle E_{\text{OV}_2}, E_{\text{OV}_2}\rangle} \tag{6}$$

in which

$$\langle E_{\text{OV}_1}, E_{\text{OV}_2}\rangle = \sum_{k_x,k_x} |E^*_{\text{OV}_1}(k_x, k_y)\cdot E_{\text{OV}_2}(k_x, k_y)|^2 \tag{7}$$

represents the cross-correlation of the far-field responses for two different OV values, namely, $\text{OV}_1 = 0$ nm and $\text{OV}_2 = 5$ nm along the positive x direction. The idea behind this cost function is, that target designs minimizing Φ will cause the most changes of the scattering signature as a function of OV and, therefore, enhance OV sensitivity. The spatial misalignment in the OV target generating E_{OV_2} causes a phase shift between the scattered waves originating from the bottom and top grating, which in turn alters their Fourier plane interference pattern. Since this spatial misalignment is only 5 nm (1/100 of the pitch), the observable effect on the interference pattern is expected to be relatively small. Therefore, we expect that E_{OV_1} and E_{OV_2} are highly correlated, which is why, even for the globally optimum scattering target, the value of the cost function should be only slightly reduced from 1. We note that the performance of the Monte Carlo technique for finding global minimums is in itself not dependent on the cost-function contrast.

We constrain ourselves to identical particle arrangements in both particle planes and start from a random distribution of particles given a particular lattice fill fraction. We generate new designs by randomly permuting filled and empty lattice sites. For each design, we compute the far-field response for the two OV values and evaluate the cost function according to eq 6. The probability of accepting a new configuration depends on the change in the cost function ΔΦ caused by the rearrangement of one particle. While in the case of $\Delta\Phi \leq 0$ the new configuration is automatically accepted, for $\Delta\Phi > 0$, the acceptance probability is calculated as follows:

$$P(\Delta\Phi) = e^{-\Delta\Phi/T} \tag{8}$$

where the control parameter T is referred to as the annealing temperature and is used to tune the acceptance probability of new candidate solutions with higher cost functions.

We choose a fixed number of iterations N_{iter} over which we quench the temperature from $T_{\max}$ to $T_{\min}$, so that at iteration step n the temperature reads

https://dx.doi.org/10.1021/acsphotonics.0c00911
ACS Photonics 2020, 7, 2765−2777

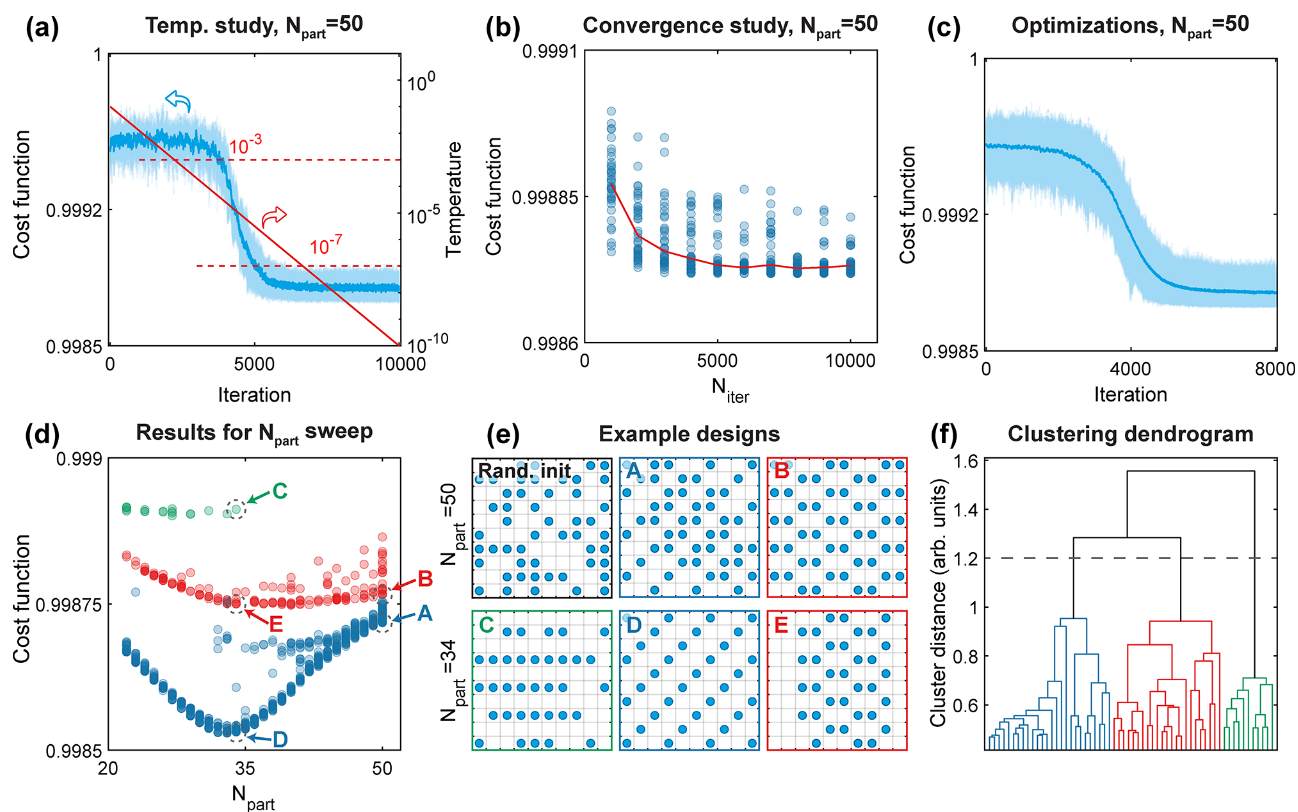

Figure 4. Overlay target optimizations. (a) Selection of optimal temperatures for a simulated annealing approach by considering 12 optimizations with N_{part} = 50. The averaged cost function is shown in dark blue. (b) Selection of an optimal cooling rate for target optimizations with N_{part} = 50, where 36 optimizations were run per N_{iter}. The solid red line represents the median value. (c) Cost function evolution, for optimal optimization settings with N_{part} = 50. The light blue lines show 150 superimposed optimizations and the dark blue line shows their average. (d) Converged cost function as a function of N_{part}. The results are color-coded with respect to a 2D FFT-based hierarchical clustering we used to identify different lattice types. (e) Examples of a randomly initiated geometry with N_{part} = 50 and optimized results for N_{part} = 50 and 34, respectively. Designs A and D are diagonal-type arrays. Designs B and E are alternating-type arrays. Design C is a rectangular array. (f) Dendrogram of the 2D FFT-based hierarchical clustering performed on the optimization results (the subtree line colors match the corresponding design families in (d)). The horizontal dashed line indicates the cutoff distance we used.

$$T(n) = T_{max}\left(\frac{T_{min}}{T_{max}}\right)^{n/N_{iter}} \tag{9}$$

To find the optimal values for T_{max} and T_{min}, we follow the parameter-selection strategy used in ref 24. To this end, we perform the temperature study shown in Figure 4a, where we run 12 optimizations (superimposed light blue lines) with N_{part} = 50 particles per layer and N_{iter} = 10^4. The average cost function is shown in dark blue. The temperature is exponentially decaying in the range between T_{max} = 10^{-1} and T_{min} = 10^{-10}. We see that, for large temperatures ($T > 10^{-3}$), any change in the OV target design is accepted, and the cost function fluctuates around the same higher values. For intermediate temperatures ($10^{-7} \leq T \leq 10^{-3}$), the cost function is effectively minimized, with a probability of converging to the global minimum. For temperatures $T < 10^{-7}$, the algorithm can only converge to local minima. After selecting the temperature extremes to be T_{max} = 10^{-3} and T_{min} = 10^{-7}, we investigate the role of the cooling rate. We do this by varying the maximum number of iterations N_{iter} while keeping the temperature extremes T_{max} and T_{min} fixed. In Figure 4b, we show the final cost function values of 36 optimization runs for each N_{iter}, where the red line represents the median value. Following this, we selected a cooling rate associated with N_{iter} = 8000 iterations and performed 150 optimizations using the chosen parameter settings, see Figure 4c for a convergence history of all solutions. We find that the results converge to two optimal particle distribution families, diagonal and alternating lattices, which account for about 85% and 15% of the results, respectively, see geometries A and B in Figure 4e. While we do observe small variations from these optimal lattices, associated with the misplacement of a few particles, we found a clear distinction between the two solutions in terms of cost function.

Next, we investigate whether these solutions also emerge for different numbers of particles by performing optimizations with a particle number N_{part} varying from 22 to 49, while using the same optimization parameters as for the study in Figure 4c. At each N_{part}, 36 optimizations are completed. In Figure 4d, all final cost function values are shown as a function of N_{part}, including the 150 results obtained for N_{part} = 50. In order to group similar geometries of particle arrangements, we perform a weighted-average distance hierarchical clustering of the absolute value of the 2D fast Fourier transform (FFT) of the particle positions. This cluster analysis was able to identify three different design families, which we colored in blue, red, and green in Figure 4d. We refer to these solution families as diagonal, alternating, and rectangular lattices, see Figure 4e, geometries D, B, and C, respectively. The dendrogram in Figure 4f depicts the results of the cluster analysis. For clarity,

we limited the number of leaves to 70. The horizontal dashed line indicates the employed cutoff distance of 1.2. As can be seen in Figure 4d, the three solution families persist for a varying number of particles, whereby the rectangular design is only found up to a particle number of N_{part} = 34, see Figure 4e, geometry C. When going from low to high particle numbers, the grid is gradually filled. In the case of the diagonal lattice for N_{part} > 34, the optimization introduces defects to the optimal solution in order to accommodate more particles, see Figure 4e, geometry A. The alternating lattice design shows a similar behavior, where for N_{part} = [30−50], suboptimal solutions emerge, which are characterized by a higher cost function and a more irregular particle arrangement. The global optimum of the optimizations in Figure 4d, which corresponds to an OV target with minimal correlations between the far-fields at OV values OV_1 = 0 nm and OV_2 = 5 nm, is a diagonal lattice with N_{part} = 34 particles, see Figure 4e, geometry D.

■ UNCERTAINTY ANALYSIS RESULTS

Design Overview. Figure 5 gives an overview of all the overlay designs and their scattering patterns that we consider in this work. The designs are classified as being essentially 1D-like, 2D-periodic, and 2D-aperiodic. The class of 1D designs includes the 1D line grating, which was approximated using a very dense arrangement of Mie spheres with a distance of 150 nm in the y direction and the same pitch p = 500 nm in the x direction. Furthermore, this class of gratings includes the rectangular and diagonal designs that emerged from the optimization study. Compared to geometry C in Figure 4e, the rectangular lattice was completed to fill the whole grid. While the 1D line grating generates just two diffraction orders, all other designs in Figure 5 result in more complex Fourier-plane light distributions, generally showing a multitude of (quasi)-diffraction orders. Qualitatively, the smallest and largest interparticle distances determine the largest and smallest diffraction angles respectively. This behavior can be easily observed in case of the rectangular and diagonal target diffraction patterns.

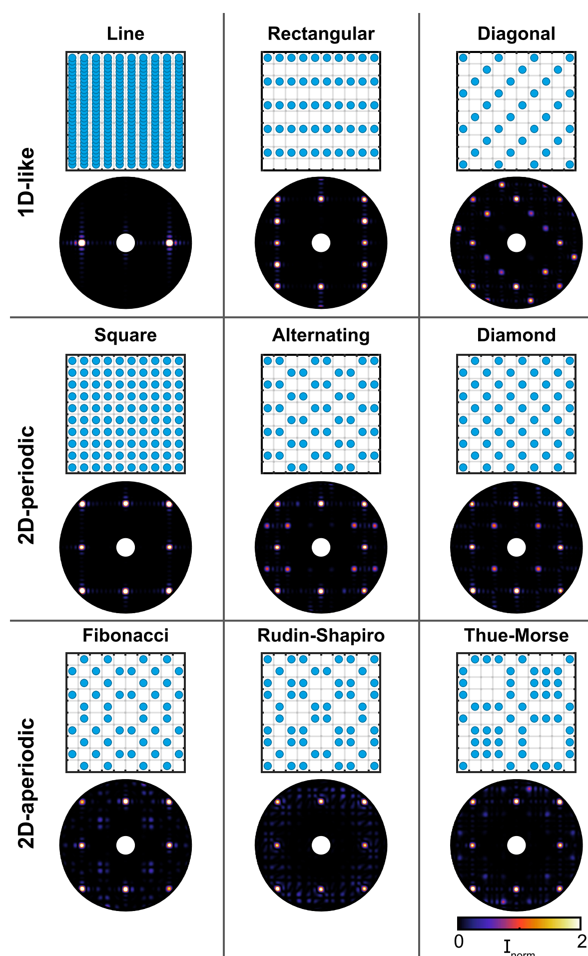

Figure 5. Designs overview. Overview of investigated OV target designs with the corresponding masked and normalized Fourier intensity profiles.

In addition to 2D-periodic designs, which include the square (all lattice sites occupied), the alternating (from optimization), and the diamond design, we have considered 2D-aperiodic targets generated from deterministic design rules. Deterministically aperiodic plasmonic and dielectric arrays have been studied in the context of scattering, fluorescence control, and lasing.[19−22] On the basis of a square lattice, one can generate designs according to, for example, the Fibonacci, Rudin−Shapiro, and Thue−Morse number sequences, as described in ref 19. The limitation to a finite size of only 10 × 10 scatterers prevents the full development of the Fourier patterns one would expect for their nearly infinitely-sized counterparts. Furthermore, we require the targets to maintain a 180° rotational symmetry, which is commonly utilized for calibration purposes. This calibration makes use of the fact that, upon a 180° target rotation, only the sign of the OV shift is flipped to remove any additional tool-induced errors, for example, lens or illumination imperfections from the scattering signature.[33] In case of the deterministically aperiodic designs, the 180° symmetry was achieved though a careful choice of the 10 × 10 truncation region from a larger aperiodic lattice. Surprisingly, the completed optimization designs already obey this rotational symmetry constraint, without the need of enforcing it during the optimization.

Shot Noise Robustness. In Figure 6a, we examine the effect of shot noise on the variance $\sigma_{\Delta OV}$ for the OV range of [−10, 10] nm. The amount of shot noise is controlled by normalizing the sample images to a certain photon budget, which here is specified as the average count per pixel $C_{avg} = 2^l$, where l = 5, 6, ..., 20, and applying Poisson noise to the Fourier images. A lower photon count results in more shot noise, which leads to higher $\sigma_{\Delta OV}$ values. For large enough photon counts, all lattice geometries converge toward an essentially zero $\sigma_{\Delta OV}$ (limited by the OV library step size of $OV_{interp,\ step}$ = 0.001 nm). The colored curves in Figure 6a correspond to different target designs and are sorted according to their $\sigma_{\Delta OV}$ values at C_{avg} = 128. The idea behind this comparison is that a faster convergence speed implies a better robustness to shot noise. The results in Figure 6c, which show the $\sigma_{\Delta OV}$ values at C_{avg} = 128, suggest that the line grating design has a vastly superior shot noise performance compared to the other designs. This outcome is not surprising from the viewpoint that the Fourier intensity signal of the line grating is concentrated to a fewer pixels as compared to other target designs, which decreases the impact of shot noise. The three optimized designs (rectangular, diagonal, and alternating) follow on positions 2−4 after the 1D line grating (which itself is not captured by the design space of the optimization). Figure 6b depicts a similar shot noise robustness study, but for a scenario where OV tolerances are much more relaxed and one

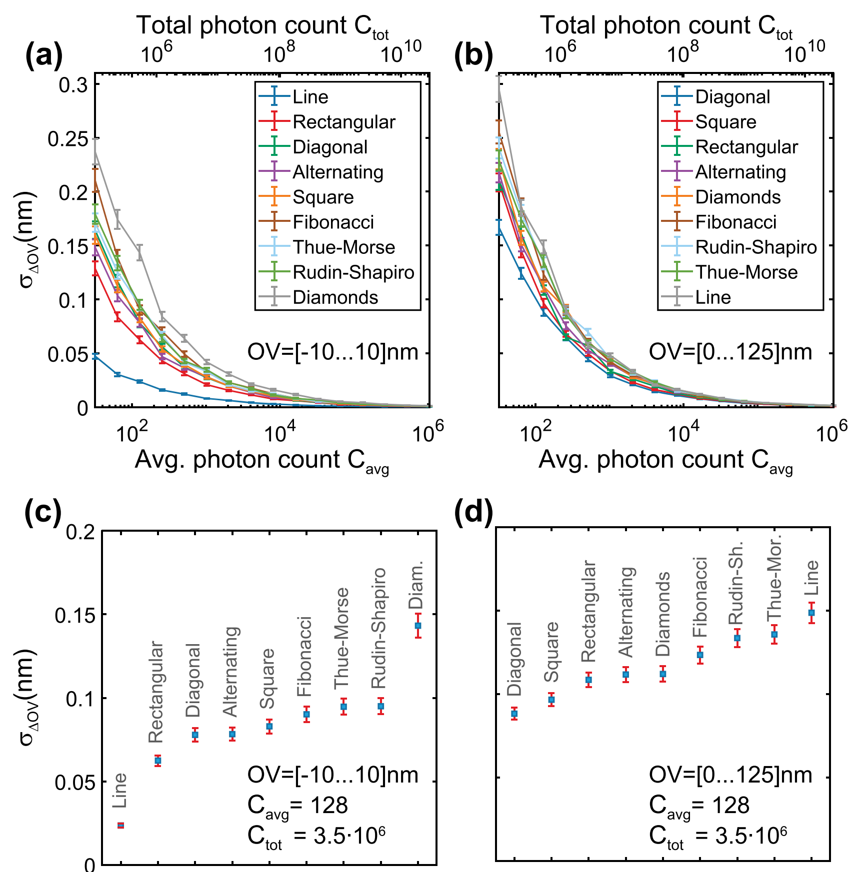

Figure 6. Shot noise robustness. (a, b) Photon count-dependent OV error variance ($\sigma_{\Delta OV}$) for the OV range of [−10−10] nm and [0−125] nm. The error bars denote the standard deviation of the variance ($\Delta\sigma_{\Delta OV}$) obtained from a half-Gaussian fit. (c, d) $\sigma_{\Delta OV}$ and $\Delta\sigma_{\Delta OV}$ values of the different OV targets at C_{avg} = 128 for the OV range of [−10−10] nm and [0−125] nm, respectively.

aims to determine OV in a 125 nm range. These type of tolerances can occur during lithography steps of noncritical wafer layers. This time the results at C_{avg} = 128 in Figure 6d feature overall larger and less-distributed $\sigma_{\Delta OV}$ values. In addition, the line target does not show the best performance anymore. Instead, the diagonal target design is superior for large overlay ranges.

An additional factor causing the overall low $\sigma_{\Delta OV}$ values presented here is the noise reducing ability of the SVD algorithm. This is due to the fact that the noisy part of the data tends to be encoded in the higher eigenvectors, which were truncated during the library creation step. This property of the SVD is often employed for noise filtering in the digital signal and image processing applications.[47] At the same time, as mentioned in the library generation section, the SVD-based approach does allow the leverage of information encoded in multiple basis functions, as opposed to only looking at the asymmetry between first diffraction orders, which benefits the OV detection at larger OV values.

Fabrication Noise Robustness. The overall high OV detection accuracy (low $\sigma_{\Delta OV}$ values) in the shot noise study can be primarily attributed to the large amount of a priori information on, for example, the array pitch, layer distance, radius, and refractive indices that is assumed in the library generation. In an experimental setting, uncertainties in these parameters, that is, fabrication noise instead of detection shot noise, is often the dominating error source. In this section, we examine the impact of three different sources of fabrication noise on the OV estimation accuracy. Process variability and imperfections of the product stack are reported to be the dominating source of error in scatterometry.[1,5] Mitigating these systematic error sources is therefore of high interest for the semiconductor industry. To distinguish between the different detrimental effects, we perform separate studies for the three different fabrication noise sources and do not introduce shot noise. As in the shot noise study, the fabrication noise is introduced to the sampling data, while we use the same libraries with the OV range of [−10, 10] nm and OV as its only input parameter.

Figure 7a depicts OV uncertainty results in case the distance between the two lattices is fluctuating with a variance of σ_t = 20 nm, which corresponds to 5% of the average layer distance t = 400 nm. Next, Figure 7b shows OV uncertainty results with particle position variations $\sigma_{\Delta x}$ = 2.5 nm, which corresponds to 0.5% of the lattice pitch. The schematics in the inset of Figure 7b show such position fluctuations, but exaggerated by a factor of 15 for visual clarity. Note, in the case of the line grating, instead of fluctuating the position of every particle, we fluctuated the positions of the 10 complete lines. Lastly, Figure 7c shows OV uncertainty results in case of particle radius variations with $\sigma_{\Delta r}$ = 7.5 nm, which corresponds to 5% of the radius. The result of the radius variation study for the diamond design is $\sigma_{\Delta OV}$ = 2.4 ± 0.1 nm, which is surprisingly high. It is omitted from the plot in Figure 7c, as it otherwise would skew the plot range for this data set. Figure 7d−f show histograms of the 300 layer distance, position error, and particle radius values used for these fabrication robustness studies.

https://dx.doi.org/10.1021/acsphotonics.0c00911
ACS Photonics 2020, 7, 2765−2777

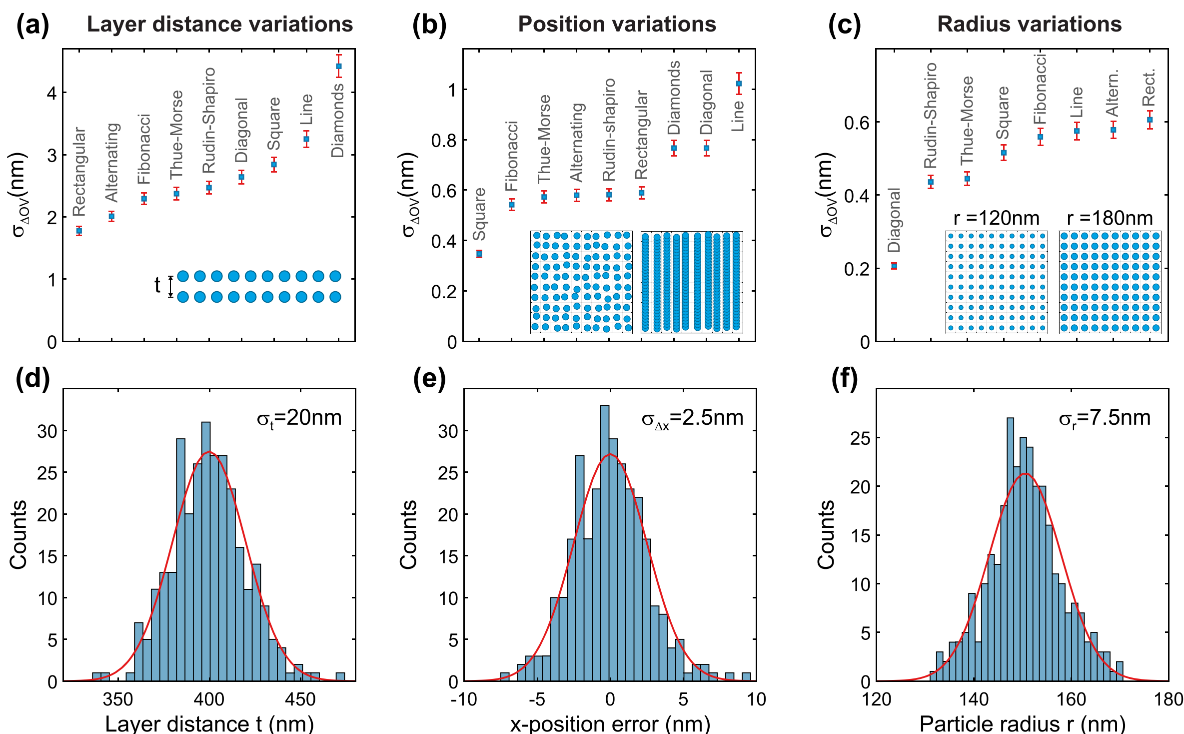

Figure 7. Fabrication noise robustness. (a−c) OV error variance results of different OV targets in case of layer distance fluctuations with a variance of σ_t = 20 nm (a), particle position fluctuations with a variance of $\sigma_{\Delta x}$ = 2.5 nm (b), and radius fluctuations with a variance of σ_r = 7.5 nm (c). The insets in (a)−(c) depict the respective situations schematically. The position fluctuations in the inset of panel (b) were increased by a factor of 15 for visual clarity. (d−f) Histograms displaying the distribution of the fluctuations of layer distance (d), particle positions (e), and radius (f). The red line in the histograms is a Gaussian fit.

The results carry several messages. First, different fabrication error sources can be partially mitigated by using a particular target design, whereby the most suited design is different for each error type. Out of the three fabrication error sources investigated here, the 5% layer distance fluctuations have resulted in the most severe impact on OV determination. Therefore, the rectangular lattice might be the most suited target design for OV metrology applications, where other types of errors are negligible. A second message is that, when one wants to be robust against multiple fabrication error sources at the same time, combining the scatterometry measurements with multiple target designs, that is, rectangular, square, and diagonal target designs, could be advantageous. Furthermore, by expanding the library parameter space, one could simultaneously determine overlay and dimensional variations (CD metrology; here, radius variations are the "critical dimension"). A third observation is that it is not obvious from the results by which mechanism a given target is more advantageous than another and why optimality depends on the source of error considered.

While it is not our ambition to explain for each scattering structure the origin of its robustness to a given disorder, we can provide a generic insight on how to leverage the SVD analysis approach for optimizing robustness/sensitivity. To exemplify this, we have performed simulation sweeps, where we continuously varied the layer thickness t in a range of [300, 500] nm and OV in a range of [−100, 100] nm for the rectangular and square geometry that are, respectively, optimal and quite poor in robustness. Using SVD, we first determine the optimal eigenbasis for the t = 400 nm data set before projecting the complete data set into this eigenspace. As an example, we show the first two projected coordinates $\mathbf{y}_j$ for the rectangular and square lattice in Figure 8 as a function of OV and t. A large sensitivity to overlay comes with a large $|\partial \mathbf{y}_j/\partial \mathrm{OV}|$, that is, a large left−right gradient in the projected coordinate. At the same time, robustness against fabrication error requires a flat dependence on t, that is, no derivative $|\partial \mathbf{y}_j/\partial t|$. Examining $\mathbf{y}_1$ in Figure 8a,b, we conclude that the higher robustness to t fluctuations of the rectangular lattice traces back to the more flat distribution of $\mathbf{y}_1$ as a function of t in the parameter region t = [350, 450] nm. Further, Figure 8e,f shows the same plots but for the second projected coordinate $\mathbf{y}_2$, which in our suggested OV determination method is expected to provide additional information on top of just the first coordinate. For both target designs at hand, $\mathbf{y}_1$ is most important for OV determination at small OV values ($|\mathrm{OV}| < 50$ nm), while $\mathbf{y}_2$ becomes more important at larger OV values. In general, the $|\partial \mathbf{y}_j/\partial \mathrm{OV}|$ plots show which parameter ranges have the highest OV sensitivity. In particular, one can identify parameter regions, which have zero OV sensitivity ($|\partial \mathbf{y}_j/\partial \mathrm{OV}| = 0$) and should therefore be avoided, since the solution of the inverse Fourier scatterometry problem is not unique.

Returning to our survey of structures in Figure 7, we note that the results with a fixed choice of target and illumination parameters presented here by no means imply that any of the proposed structures are working at their optimum in parameter space. While outside of the scope of this work, such optimal parameters can be found by performing separate multi-parametric SVD analysis, as shown in Figure 8 for each target design and each parameter combination. Thus, the presented results on performance variability between structures are to some degree incidental. However, the results highlight the importance of target design, which is often neglected in other OV metrology studies. Note that, in practice, there are several

https://dx.doi.org/10.1021/acsphotonics.0c00911
ACS Photonics 2020, 7, 2765−2777

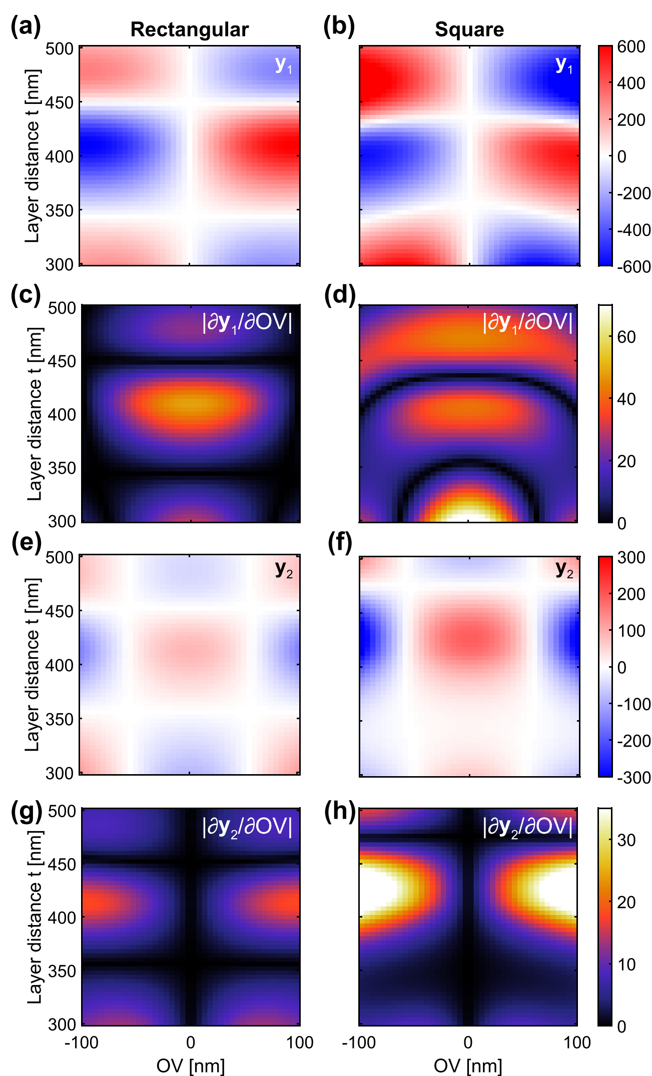

Figure 8. Parameter sweep. (a, b) Eigenbasis projection $\mathbf{y}_1$ as a function of layer distance t for the rectangular and square target, respectively. (c, d) Absolute valued partial derivative of (a) and (b) with respect to OV. (e−h) Same as (a)−(d) but for the second eigenbasis projection $\mathbf{y}_2$.

ways to decrease the impact of systematic errors, such as fabrication imperfections, to achieve lower $\sigma_{\Delta OV}$ numbers than the ones reported in Figure 7. One common way to mitigate imperfections is to include them in the library as an input and, therefore, a fitting parameter for the sampling data. This would, in turn, increase the complexity of the library creation and library search process. Another approach to mitigate systematic OV errors is the fabrication and measurement of two neighboring OV targets with known programmed overlay.[4] In addition, while we assumed single shot measurements, combining several measurements with a varying angle of incidence, polarization, or wavelength can offer benefits for OV metrology. Such approaches are reported to not only increase the amount of available information, but also improve process robustness.[48]

CONCLUSION AND OUTLOOK

In summary, we presented a new method for characterizing the performance of overlay metrology based on nonperiodic 2D Fourier scatterometry target designs, three of which resulted from simulated annealing optimizations, and others were chosen as quasiperiodic motifs. The workflow consists of SVD analysis in order to convert a library of simulated "reference" diffraction patterns at known overlays into an optimal basis onto which one should project measurements at an unknown overlay for the most efficient determination of OV. We demonstrated, based on rigorous electromagnetic simulations, in combination with a statistical Monte Carlo method, how one can assess an overlay estimation uncertainty in the face of measurement noise and robustness against nanofabrication disorder. The results suggest that 2D OV target designs might be a promising alternative to line gratings regarding some of the OV metrology challenges, such as systematic errors due to fabrication variations. One possible way to take advantage of the findings would be to perform OV measurements with multiple target designs, which have complementary fabrication noise robustness properties. Combinations would allow to simultaneously optimize robustness, sensitivity, range of OV detection, and multiplexing OV and CD detection.

In real-world conditions, the reported levels of uncertainty would likely be difficult to achieve because of the large amount of required measurements and precision with which the "true" OV needs to be known to construct the library. This underlines the importance of simulations for library construction. Our work demonstrates the strength of semi-analytical calculations for proof-of-principle metrology studies as compared to discretization-based full-wave solvers. Our tests have shown that, for instance, FDTD tends to introduce meshing-based errors that far exceed the diffraction pattern variations that are induced by the overlay values of interest. While in this work we used the generalized Mie theory approach that is limited to spherical particles in free space, we foresee a large role for multipole multiple scattering methods for scatterers in stratified media,[49] and the boundary element method in layered systems[50] in order to increase the realism of the simulations, yet avoiding impractically difficult gridding in FDTD/FEM.

As an outlook, the OV target design space used in this work could be further extended. For instance, we chose identical designs for the bottom and top gratings, whereas in fact the strength of, for example, quasicrystal motifs is that different tiles cut out from a quasicrystal share similar diffraction patterns in terms of amplitude, but have differences in phase. It could, hence, be advantageous to, for example, choose different tiles from the same lattice family as the lower and upper grating. Also, instead of using a fixed periodic lattice as the underlying template on which to place particles, one could consider continuous particle placements to optimize diffraction pattern correlations, in the vein of work on plasmonic Vogel spirals and hyperuniform designs.[51−53] Regarding numerical optimizations to generate designs, an outstanding challenge is to define the most effective cost function and optimization approaches, so as to optimize sensitivity, OV range, to multiplex OV and CD sensitivity, and to multiplex sensitivity to OV in both directions. Finally, using the presented uncertainty estimation approach, one could study more complex measurement schemes that involve capturing signals at multiple wavelengths, multiple polarizations, or introducing phase sensitivity, which would increase the captured information content and allow a more elaborate mitigation of systematic error sources.

https://dx.doi.org/10.1021/acsphotonics.0c00911
ACS Photonics 2020, 7, 2765−2777

AUTHOR INFORMATION

Corresponding Author

A. Femius Koenderink − *AMOLF, 1098 XG Amsterdam, The Netherlands;* orcid.org/0000-0003-1617-5748; Email: f.koenderink@amolf.nl

Authors

Ruslan Röhrich − *AMOLF, 1098 XG Amsterdam, The Netherlands; ARCNL, 1098 XG Amsterdam, The Netherlands*
Giorgio Oliveri − *AMOLF, 1098 XG Amsterdam, The Netherlands*
Stefanos Kovaios − *AMOLF, 1098 XG Amsterdam, The Netherlands*
Vasco T. Tenner − *ARCNL, 1098 XG Amsterdam, The Netherlands; Department of Physics and Astronomy, and LaserLaB, Vrije Universiteit, 1081 HV Amsterdam, The Netherlands; ASML Netherlands B.V., 5504 DR Veldhoven, The Netherlands*
Arie J. den Boef − *ARCNL, 1098 XG Amsterdam, The Netherlands; Department of Physics and Astronomy, and LaserLaB, Vrije Universiteit, 1081 HV Amsterdam, The Netherlands; ASML Netherlands B.V., 5504 DR Veldhoven, The Netherlands*
Johannes T. B. Overvelde − *AMOLF, 1098 XG Amsterdam, The Netherlands*

Complete contact information is available at:
https://pubs.acs.org/10.1021/acsphotonics.0c00911

Notes

The authors declare no competing financial interest.

ACKNOWLEDGMENTS

The authors thank N. Schilder and J. P. Hugonin for providing the GLMT simulation code. We also thank L. Loetgering, C. Messinis, and J. F. de Boer for useful discussions. This work is part of the research programme of the Dutch Research Council (NWO) and was performed at the research institute AMOLF, as well as at ARCNL, a public−private partnership of UvA, VU, NWO, and ASML.

REFERENCES

(1) Bunday, B.; Solecky, E.; Vaid, A.; Bello, A.; Dai, X. Metrology capabilities and needs for 7nm and 5nm logic nodes. *Proc. SPIE* **2017**, *10145*, 101450G.
(2) Orji, N. G.; Badaroglu, M.; Barnes, B. M.; Beitia, C.; Bunday, B. D.; Celano, U.; Kline, R. J.; Neisser, M.; Obeng, Y.; Vladar, A. Metrology for the next generation of semiconductor devices. *Nat. Electron.* **2018**, *1*, 532−547.
(3) Madsen, M. H.; Hansen, P.-E. Scatterometry—fast and robust measurements of nano-textured surfaces. *Surf. Topogr.: Metrol. Prop.* **2016**, *4*, 023003.
(4) den Boef, A. J. Optical wafer metrology sensors for process-robust CD and overlay control in semiconductor device manufacturing. *Surf. Topogr.: Metrol. Prop.* **2016**, *4*, 023001.
(5) Bhattacharyya, K.; den Boef, A. J.; Storms, G.; van Heijst, J.; Noot, M.; An, K.; Park, N.-K.; Jeon, S.-R.; Oh, N.-L.; McNamara, E.; van de Mast, F.; Oh, S.; Lee, S. Y.; Hwang, C.; Lee, K. A study of swing-curve physics in diffraction-based overlay. *Proc. SPIE* **2016**, *9778*, 97781I.
(6) Bishop, K. P.; Gaspar, S. M.; Milner, L.-M.; Naqvi, S. S. H.; McNeil, J. R. Grating line shape characterization using scatterometry. *Proc. SPIE* **1991**, *1545*, 64−73.
(7) Lee, M.; Galarza, C.; Kong, W.; Sun, W.; Terry, F., Jr Analysis of reflectometry and ellipsometry data from patterned structures. *AIP Conf. Proc.* **1998**, *449*, 331−335.
(8) Niu, X.; Jakatdar, N.; Bao, J.; Spanos, C. J. Specular spectroscopic scatterometry. *IEEE Trans. Semicond. Manuf.* **2001**, *14*, 97−111.
(9) Yang, W.; Lowe-Webb, R.; Rabello, S.; Hu, J.; Lin, J.-Y.; Heaton, J. D.; Dusa, M. V.; den Boef, A. J.; van der Schaar, M.; Hunter, A. Novel diffraction-based spectroscopic method for overlay metrology. *Proc. SPIE* **2003**, *5038*, 200−207.
(10) Petit, J.; Boher, P.; Leroux, T.; Barritault, P.; Hazart, J.; Chaton, P. Improved CD and overlay metrology using an optical Fourier transform instrument. *Proc. SPIE* **2005**, *5752*, 420−428.
(11) Patrick, H. J.; Attota, R.; Barnes, B. M.; Germer, T. A.; Dixson, R. G.; Stocker, M. D.; Silver, R. M.; Bishop, M. R. Optical critical dimension measurement of silicon grating targets using back focal plane scatterfield microscopy. *J. Micro/Nanolithogr., MEMS, MOEMS* **2008**, *7*, 013012.
(12) Fallet, C.; Novikova, T.; Foldyna, M.; Manhas, S.; Ibrahim, B. H.; De Martino, A.; Vannuffel, C.; Constancias, C. Overlay measurements by Mueller polarimetry in back focal plane. *J. Micro/Nanolithogr., MEMS, MOEMS* **2011**, *10*, 1−8.
(13) Paz, V. F.; Peterhänsel, S.; Frenner, K.; Osten, W. Solving the inverse grating problem by white light interference Fourier scatterometry. *Light: Sci. Appl.* **2012**, *1*, No. e36.
(14) Madsen, M. H.; Boher, P.; Hansen, P.-E.; Jørgensen, J. F. Alignment-free characterization of 2D gratings. *Appl. Opt.* **2016**, *55*, 317−322.
(15) Röhrich, R.; Hoekmeijer, C.; Osorio, C. I.; Koenderink, A. F. Quantifying single plasmonic nanostructure far-fields with interferometric and polarimetric k-space microscopy. *Light: Sci. Appl.* **2018**, *7*, 65.
(16) Polman, A.; Atwater, H. A. Photonic design principles for ultrahigh-efficiency photovoltaics. *Nat. Mater.* **2012**, *11*, 174−177.
(17) Arbabi, A.; Horie, Y.; Bagheri, M.; Faraon, A. Dielectric metasurfaces for complete control of phase and polarization with subwavelength spatial resolution and high transmission. *Nat. Nanotechnol.* **2015**, *10*, 937.
(18) Koenderink, A. F.; Alù, A.; Polman, A. Nanophotonics: Shrinking light-based technology. *Science* **2015**, *348*, 516−521.
(19) Dal Negro, L.; Feng, N.-N.; Gopinath, A. Electromagnetic coupling and plasmon localization in deterministic aperiodic arrays. *J. Opt. A: Pure Appl. Opt.* **2008**, *10*, 064013.
(20) Dal Negro, L.; Boriskina, S. V. Deterministic aperiodic nanostructures for photonics and plasmonics applications. *Laser Photonics Rev.* **2012**, *6*, 178−218.
(21) Wiersma, D. S. Disordered photonics. *Nat. Photonics* **2013**, *7*, 188.
(22) Schokker, A. H.; Koenderink, A. F. Lasing in quasi-periodic and aperiodic plasmon lattices. *Optica* **2016**, *3*, 686−693.
(23) Kirkpatrick, S.; Gelatt, C. D.; Vecchi, M. P. Optimization by simulated annealing. *Science* **1983**, *220*, 671−680.
(24) Oliveri, G.; Overvelde, J. T. Inverse design of mechanical metamaterials that undergo buckling. *Adv. Funct. Mater.* **2020**, *30*, 1909033.
(25) Gross, H.; Model, R.; Bär, M.; Wurm, M.; Bodermann, B.; Rathsfeld, A. Mathematical modelling of indirect measurements in scatterometry. *Measurement* **2006**, *39*, 782−794.
(26) Sigmund, O.; Maute, K. Topology optimization approaches. *Struct. Multidiscip. Optim.* **2013**, *48*, 1031−1055.
(27) Molesky, S.; Lin, Z.; Piggott, A. Y.; Jin, W.; Vucković, J.; Rodriguez, A. W. Inverse design in nanophotonics. *Nat. Photonics* **2018**, *12*, 659−670.
(28) Schneider, P.-I.; Garcia Santiago, X.; Soltwisch, V.; Hammerschmidt, M.; Burger, S.; Rockstuhl, C. Benchmarking five global optimization approaches for nano-optical shape optimization and parameter reconstruction. *ACS Photonics* **2019**, *6*, 2726−2733.
(29) Sirovich, L.; Kirby, M. Low-dimensional procedure for the characterization of human faces. *J. Opt. Soc. Am. A* **1987**, *4*, 519−524.

(30) Turk, M.; Pentland, A. Eigenfaces for recognition. *J. Cognit. Neurosci.* **1991**, *3*, 71−86.
(31) di Francia, G. T. Resolving power and information. *J. Opt. Soc. Am.* **1955**, *45*, 497−501.
(32) Moharam, M. G.; Gaylord, T. K. Rigorous coupled-wave analysis of planar-grating diffraction. *J. Opt. Soc. Am.* **1981**, *71*, 811−818.
(33) Chen, X.; Liu, S. In *Metrology*; Gao, W., Ed.; Springer: Singapore, 2019; pp 1−37.
(34) Pisarenco, M.; Maubach, J.; Setija, I.; Mattheij, R. Aperiodic Fourier modal method in contrast-field formulation for simulation of scattering from finite structures. *J. Opt. Soc. Am. A* **2010**, *27*, 2423−2431.
(35) Silver, R. M.; Attota, R.; Marx, E. Model-based analysis of the limits of optical metrology with experimental comparisons. *Proc. SPIE* **2007**, *6617*, 66170W.
(36) Xu, B.; Ma, L.; Zou, X.; Dong, L.; Wei, Y. A diffraction-based overlay model based on FDTD method. *Proc. SPIE* **2019**, *10959*, 109592X.
(37) van der Hulst, H. C. *Light Scattering by Small Particles*; Dover books on physics; Dover: New York, NY, 1981.
(38) Stout, B.; Auger, J.-C.; Lafait, J. A transfer matrix approach to local field calculations in multiple-scattering problems. *J. Mod. Opt.* **2002**, *49*, 2129−2152.
(39) Pierce, D. T.; Spicer, W. E. Electronic structure of amorphous Si from photoemission and optical studies. *Phys. Rev. B* **1972**, *5*, 3017−3029.
(40) Raymond, C. J.; Littau, M. E.; Chuprin, A.; Ward, S. Comparison of solutions to the scatterometry inverse problem. *Proc. SPIE* **2004**, *5375*, 564−575.
(41) Schwenke, H.; Siebert, B.; Wäldele, F.; Kunzmann, H. Assessment of uncertainties in dimensional metrology by Monte Carlo simulation: proposal of a modular and visual software. *CIRP Ann.* **2000**, *49*, 395−398.
(42) Arnz, M.; Klose, G.; Troll, G.; Beyer, D.; Mueller, A. Monte-Carlo simulations of image analysis for flexible and high-resolution registration metrology. *Proc. SPIE* **2009**, *7470*, 74700L.
(43) McKay, M. D.; Beckman, R. J.; Conover, W. J. Comparison of three methods for selecting values of input variables in the analysis of output from a computer code. *Technometrics* **1979**, *21*, 239−245.
(44) Helton, J. C.; Davis, F. J. Latin hypercube sampling and the propagation of uncertainty in analyses of complex systems. *Reliab. Eng. Syst. Saf.* **2003**, *81*, 23−69.
(45) Heidenreich, S.; Gross, H.; Bär, M.; Wright, L. Uncertainty propagation in computationally expensive models: A survey of sampling methods and application to scatterometry. *Measurement* **2017**, *97*, 79−87.
(46) Yang, J. Convergence and uncertainty analyses in Monte-Carlo based sensitivity analysis. *Environ. Modell. Software* **2011**, *26*, 444−457.
(47) Konstantinides, K.; Natarajan, B.; Yovanof, G. S. Noise estimation and filtering using block-based singular value decomposition. *IEEE Trans. Image Process.* **1997**, *6*, 479−483.
(48) Bhattacharyya, K.; Noot, M.; Chang, H.; Liao, S.; Chang, K.; Gosali, B.; Su, E.; Wang, C.; den Boef, A.; Fouquet, C.; Huang, G.-T.; Chen, K.-H.; Cheng, K.; Lin, J. Multi-wavelength approach towards on-product overlay accuracy and robustness. *Proc. SPIE* **2018**, *10585*, 105851F.
(49) Chen, Y. T.; Zhang, Y.; Koenderink, A. F. General point dipole theory for periodic metasurfaces: magnetoelectric scattering lattices coupled to planar photonic structures. *Opt. Express* **2017**, *25*, 21358−21378.
(50) Hohenester, U.; Trügler, A. MNPBEM - A Matlab toolbox for the simulation of plasmonic nanoparticles. *Comput. Phys. Commun.* **2012**, *183*, 370−381.
(51) Trevino, J.; Cao, H.; Dal Negro, L. Circularly symmetric light scattering from nanoplasmonic spirals. *Nano Lett.* **2011**, *11*, 2008−2016.
(52) Guo, K.; Du, M.; Osorio, C. I.; Koenderink, A. F. Broadband light scattering and photoluminescence enhancement from plasmonic Vogel's golden spirals. *Laser Photon. Rev.* **2017**, *11*, 1600235.
(53) Castro-Lopez, M.; Gaio, M.; Sellers, S.; Gkantzounis, G.; Florescu, M.; Sapienza, R. Reciprocal space engineering with hyperuniform gold disordered surfaces. *APL Photonics* **2017**, *2*, 061302.